

Aeroacoustic signatures reveal fast transient dynamics of vapor-jet-driven cavity oscillations in metallic additive manufacturing

Haolin Liu^{1,2*†}, S. Kiana Naghibzadeh^{3†}, Zhongshu Ren^{4,5,6}, Yanming Zhang⁷, Jiayun Shao⁴, Samuel J. Clark⁸, Kamel Fezzaa⁸, Xuzhe Zeng¹, Lin Gao⁹, Wentao Yan⁷, Noel Walkington¹⁰, Kaushik Dayal^{1,10,11}, Tao Sun^{4,8}, Anthony D. Rollett^{2*}, Levent Burak Kara^{1*}

Affiliations

¹Department of Mechanical Engineering, Carnegie Mellon University; Pittsburgh, PA, USA.

²Department of Materials Science and Engineering, Carnegie Mellon University; Pittsburgh, PA, USA.

³Department of Civil and Environmental Engineering, Massachusetts Institute of Technology; Cambridge, MA, USA.

⁴Department of Mechanical Engineering, Northwestern University; Evanston, IL, USA.

⁵Department of Materials Science and Engineering, University of Virginia; Charlottesville, VA, USA

⁶Physical Sciences and Research Operations Division, National Synchrotron Light Source II, Brookhaven National Laboratory; Upton, NY, USA

⁷Department of Mechanical Engineering, National University of Singapore; Singapore.

⁸X-ray Science Division, Advanced Photon Source, Argonne National Laboratory; Lemont, IL, USA.

⁹Department of Mechanical Engineering, The University of Alabama; Tuscaloosa, AL, USA.

¹⁰Center for Nonlinear Analysis, Department of Mathematical Sciences, Carnegie Mellon University; Pittsburgh, PA, USA.

¹¹Department of Civil and Environmental Engineering, Carnegie Mellon University; Pittsburgh, PA, USA.

*Corresponding authors. Email: haolinl@andrew.cmu.edu; rollett@andrew.cmu.edu; lkara@andrew.cmu.edu.

†These authors contribute equally to this work.

Summary paragraph

Aeroacoustic emissions from intense evaporation are widely measured yet often treated as noisy byproducts and used mainly in empirical monitoring¹⁻⁸. Here, we show that airborne sound encodes physics-governed sub-millisecond fingerprints of vapor-jet dynamics in excessive vaporization, exemplified by vapor keyholes in laser metal processing⁹⁻¹⁶. From first principles, we develop a vapor-jet-cavity oscillation framework and incorporate it into an aeroacoustic formulation, thereby coupling measured sound to transient cavity depth and oscillation frequency¹⁷⁻³⁰. Reconciled with synchronized multimodal in-situ data, airborne acoustics enable accurate tracking of vapor-cavity properties within tens to hundreds of microseconds. Combined with newly discovered correlations, cavity-jet-acoustic theory recasts the transition from steady, pore-free to pore-shedding vaporizations as a critical-frequency event. Aeroacoustic emissions thus become scalable, physics-guided, and cost-efficient probes of rapidly evolving liquid–vapor systems.

Airborne sound accompanies nearly every instance of rapid vaporization, a common physical process that occurs from boiling and cavitation to laser ablation and metal welding¹⁻⁵. Yet, even when acoustic emissions from excessive evaporation exhibit repeatable tonal features, the mechanisms governing how those features evolve, as well as how they map quantitatively onto momentary vaporization dynamics, remain only partially understood^{1,2,4-6}. Arising from mass and momentum exchange between vapor jets and the surrounding medium, these ubiquitous emissions are often treated as noisy, broadband, and configuration-sensitive, hence hindering mechanistic interpretation^{2,5-7}. Accordingly, despite the widespread empirical usage of acoustic sensing, a deterministic and physics-based understanding of how transient liquid–vapor motion relates to measurable airborne sound has remained elusive^{4,6-8}. This gap raises a fundamental question: *can the ubiquitous yet seemingly noisy sound of excessive vaporization encode transient physics-consistent signatures of the process itself?*

More broadly, this question concerns *observability and mechanistic attribution* in non-equilibrium intense vaporization across a wide range of scientific and engineering topics^{4,5}. Notably, laser-based metal processing (LMP), where concentrated laser energy deposition melts and resolidifies metal feedstock to produce dense components, offers a particularly tangible testbed for addressing this gap. In laser-based welding and powder bed fusion (PBF), excessive laser heating frequently occurs and drives the melt pool to temperatures near or above the alloy’s boiling point⁹. The ensuing rapid vaporization generates airborne acoustic emissions and produces a recoil pressure that depresses the liquid surface, forming a vapor-filled cavity known as a *keyhole*¹⁰. Under vigorous and highly transient evaporation, the vapor jet sustains a deep keyhole geometry while emitting sound⁸; oscillations of the deep keyhole, sometimes accompanied by intermittent collapse

and gas entrapment that shed near-spherical pores and seed defects known as keyhole porosity¹⁰, can in turn modulate the vapor jet and its associated acoustic emissions⁹⁻¹¹. Albeit a specific case, LMP couples acoustic emissions with driven vapor jets, compliant liquid cavities, and strongly time-dependent interfacial dynamics, making it representative of a broader class of vaporization-driven dynamical systems and a useful context for developing transferable observability principles.

Another crucial and impactful aspect of the aforementioned observability and interpretability hinges on *time-resolved accessibility*, namely, the extent to which they can be achieved rapidly using easily accessible, cost-effective sensing methods across diverse practical settings. In recent years, monitoring approaches spanning from high-fidelity *in situ* and *ex situ* measurements to computational and data-centric predictive models have been developed to advance evaporation-associated physical understanding and enable quantitative inference of process behaviours¹²⁻¹⁶. These approaches have been applied to resolve phase-transition dynamics, defect formation, and manufacturing outcomes in systems involving ablative evaporation¹⁴⁻¹⁶. However, many diagnostic modalities remain costly and resource intensive, limiting their ability to capture the fast transient vaporization dynamics that often govern process quality^{12,14-16}. By contrast, airborne acoustics are commonly viewed as an inexpensive indicator of process stability¹²⁻¹⁴, but aeroacoustic signatures from excessive vaporization are typically treated as indirect, low-signal-to-noise-ratio (SNR) observables and interpreted primarily through empirical rules or data-driven correlations¹⁶⁻²⁴. This limitation reflects both the sensitivity of liquid-vapor behaviors to coupled laser-driven vaporization and interfacial forces and the lack of analytical, mechanistic descriptions linking transient vapor-cavity dynamics to measurable sound generation^{10,17-20}. As a result, airborne acoustic monitoring often requires extensive condition-specific datasets^{14,16}, hindering

scalable, physics-informed monitoring strategies and efficient models for this inherently complex system^{12,19,25–28}.

In this work, we address these long-standing obstacles to deepen mechanistic understanding and broaden the practical utility of airborne acoustic emissions from rapid and excessive vaporizations. We discover and demonstrate that, despite appearing noisy and ambiguous, aeroacoustic signatures from intense evaporation encode informative, physics-governed fingerprints of vapor-jet dynamics and cavity oscillations. As illustrated in Fig. 1, we first construct a laser-PBF experimental prototype that integrates synchronized multimodal in situ characterization with a machine-learning-enabled data-processing pipeline to observe and analyze laser-induced excessive vaporization in Ti-6Al-4V alloy (Fig. 1A). Inspired by newly revealed cross-modality correlations, we develop a perturbation-based linear framework for vapor-jet–cavity oscillations and couple it with aeroacoustic formulations^{29,30} to derive a *Vapor-jet–Cavity (keyhole) Aeroacoustic Equation (VCAE)* that links aeroacoustic signatures to vapor-jet and cavity-depth accelerations, showing that measurable airborne sound encodes the underlying vapor-jet–cavity physics (Fig. 1B). Next, we extend the analysis to the nonlinear regime by deriving the *Vapor-jet–Cavity (keyhole) Oscillation Dynamics Equation (VCODE)*, a new and generalizable ordinary differential equation from continuum conservation laws that governs the transient nonlinear coupling between deep cavity-depth fluctuations and vapor-jet evolution (Fig. 1C). We reconcile these predictions and theoretical inferences with synchronized measurements, achieving qualitative agreement and enabling, for the first time, high-fidelity quantitative inference of key vaporization variables over sub-millisecond windows from airborne sound. Finally, in the context of laser-PBF, we identify in acoustic data a threshold frequency associated with the transition from steady, porosity-free keyholes (N-KH) to

pore-shedding keyholes (P-KH) in Ti-6Al-4V. Combined with our theoretical framework, this finding motivates a mechanistic reinterpretation of the keyhole defect boundary (KH-bound) on the laser power–scan speed (P – V) map¹⁹ as a critical iso-frequency contour in the same parameter space. Together, these results recast aeroacoustic signatures from vapor-jet-driven cavities as physics-informed observables, establishing a practical and cost-effective route to interrogate rapidly evolving excessive-vaporization systems using airborne acoustic emissions. By enabling accurate, rapid transient inference over time windows of a few hundred microseconds, our work leverages airborne acoustics to facilitate vaporization characterization by two to three orders of magnitude, aided by its broad generalizability, cost-effectiveness, fast response, and ease of deployment.

***In situ* multimodal prototype for characterization of laser-induced vaporization**

Our laser-induced vaporization prototype, *i.e.*, a laser-PBF platform, is equipped with synchronized *in situ* characterization modalities, including synchrotron X-ray imaging and ultrasonic airborne acoustic sensing (Fig. 1A). We performed single-track laser-melting experiments on Ti-6Al-4V using a focused laser beam across a range of laser power–scan speed (P – V) combinations to systematically probe vapor-cavity behavior. All modalities were registered to a common timeline to enable direct correlation between acoustic emissions and X-ray-resolved cavity geometry. An ultrasonic microphone was positioned near the top of the fusion zone to capture near-source acoustic signals from vapor jets exiting the cavity with minimal turbulence contamination. During processing, acoustic and other time-series signals were analyzed in the time domain and, when needed, via continuous wavelet transforms (CWT) to obtain spectro-temporal scalograms and extract spectral components. In parallel, we quantified side-view cavity profiles

using a high-accuracy U-Net³¹ segmentation model trained on only a handful of precisely manually labeled images, enabling automated cavity segmentation, contour extraction, and geometric feature quantification across the full X-ray dataset³². Together with automated cross-modality synchronization, this pipeline eliminated labor-intensive manual measurements and manual data pairing (Methods).

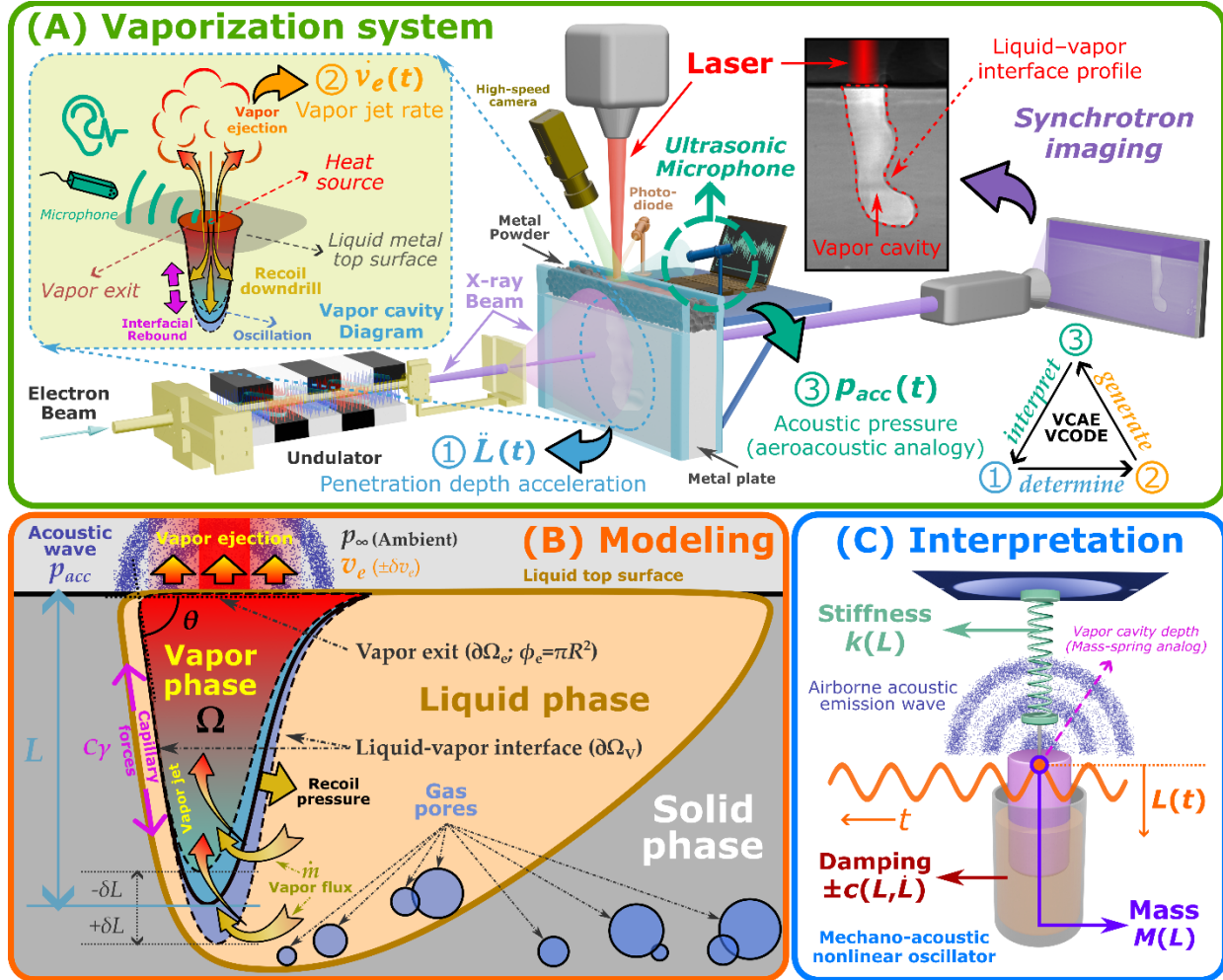


Fig. 1. Multimodal prototype and mechanistic interpretation of laser-driven excessive vaporization. (A) Vaporization paradigm and synchrotron-compatible experimental prototype. Side-view synchrotron X-ray imaging resolves transient vapor-cavity profiles, while an ultrasonic microphone records airborne pressure fluctuations emitted at the vapor exit; auxiliary sensors (e.g., infrared camera and photodiode) monitor thermal/optical signatures. The coupled process links cavity-depth acceleration ($\dot{L}(t)$), rate of vertical vapor-jet velocity ($\dot{v}_e(t)$), and radiated acoustic pressure ($p_{acc}(t)$); interpreted via acoustic formulations), enabling inference between cavity dynamics and acoustics. (B) Modeling schematic of the vapor cavity side-view highlighting recoil pressure, interfacial capillarity, and vaporization mass flux that shape the liquid–vapor interface, modulate cavity depth L , and drive oscillatory vapor ejection that produces airborne acoustic waves and can seed porosity. These considerations lead to a theoretical model

that describes transient depth evolution, constrained by time-resolved X-ray measurements of interface geometry and exit conditions. (C) Vapor-cavity depth is interpreted as a nonlinear mechano-acoustic oscillator that strongly modulates vapor ejection, the resulting sound, and its stability. The extracted oscillator model has effective mass $M(L)$, effective stiffness $k(L)$, and effective damping $c(L, \dot{L})$ with either positive or negative values, all of which are derived from vapor jet parameters and cavity's geometric properties.

After synchronization, the registered measurements were partitioned into short 400 or 800 μs snippets for subsequent correlation analysis. This synchronized snippet dataset provides a time-resolved view of excessive vaporization in which cavity geometry and airborne acoustics are measured simultaneously under systematically varied conditions. Within these snippets, cavity motion and acoustic signatures co-evolve in a very structured manner (Fig. 2A): changes in cavity depth accelerations and oscillation phase track repeatable shifts in the emitted ultrasound, indicating that the airborne signal is not merely incidental noise but an informative projection of the instantaneous cavity state. These discoveries motivate the theoretical development that follows: we use the X-ray-derived cavity evolution to formulate and constrain a first-principles, fluid-dynamics-based description of vapor-jet-driven cavity oscillations, and we use the collocated acoustic measurements to test and quantify how those dynamics are encoded in scalable airborne signatures. More details are referred to the Supplementary Information.

Coupling between vapor jet and cavity oscillations

To interpret the multimodal measurements and observations, we start from developing a rough and simple mechanistic description of steady vapor-cavity oscillation dynamics and their associated aeroacoustic emissions. Figure 1B shows the side-view profile of the vapor cavity and the depiction of the modeling framework for the mechano-acoustic system of interest. Assuming a near-cylindrical shape (Ω , also used to denote the volume) of the vapor-cavity with its depth (L)

and vapor-jet velocity (v_e) at the cavity opening ($\partial\Omega_e$) as the predominant variables, we obtain the following balance of mass equation within Ω :

$$\dot{m} = \rho_v \frac{d\Omega}{dt} + \rho_v \phi_e v_e = \rho_v \phi_e (\dot{L} + v_e) \quad (\text{Eq. 1})$$

where ρ_v and ϕ_e denote the vapor density (assumed constant for now) and area of $\partial\Omega_e$, respectively, and \dot{m} denotes the total mass vaporization rate across the liquid–vapor interface ($\partial\Omega_v$) of the vapor cavity. Equation 1 essentially states that the rate of change of mass ($\rho_v \dot{\Omega}$) within Ω equals the mass influx (\dot{m}) minus the mass outflux ($\rho_v \phi_e v_e$). During steady and pore-free oscillations observed in experiments, we have both L and v_e fluctuate with small amplitudes. Therefore, we further assume that under small geometric perturbations, \dot{m} —predominantly associated with the total laser absorption determined by the laser absorptivity and cavity’s unperturbed size and shape—remains approximately constant, *i.e.*, $\dot{m} = 0$ ^{18–20,23,33}. Guided by this interpretation and introducing small perturbations to v_e and L , *i.e.*, δv_e and δL , about their steady state v_{e0} and L_0 , we differentiate both sides of Eq. 1 with respect to time and yield $\dot{\delta v}_e = -\ddot{\delta L}$ (or $\dot{v}_e = -\ddot{L}$), revealing that under small changes of v_e and L , the time derivative of v_e is proportional to the negative of the acceleration of L . This relationship is fundamental to understanding the airborne acoustic emissions driven by the vapor jet around $\partial\Omega_e$, as subsequent analyses demonstrate that \dot{v}_e is directly proportional to the measured acoustic amplitude.

Connecting acoustic signatures with transient vaporization dynamics

During intense laser-induced vaporization, mechanical acoustic waves are generated by fluctuating jets around the vapor exit and propagate outward until they reach the ultrasonic microphone, where they are recorded as time-series signals. To investigate further the mechanism by which the airborne acoustics are generated near $\partial\Omega_e$, we use *Lighthill's aeroacoustic formulations*^{29,30} to formulize emitted acoustic signatures, which can be further connected with vapor-jet dynamics and cavity oscillations using Eq. 1. By characterizing source terms in *the Lighthill equation for aeroacoustics*²⁹ with v_e , we obtain the following expression consisting of leading terms for the resultant acoustic pressure amplitude (p_{acc}) originating from the cavity exit $\partial\Omega_e$:

$$p_{acc} - p_\infty \sim \frac{\rho_v \phi_e}{4\pi r} (2M + 1) \frac{dv_e}{dt} \quad (\text{Eq. 2})$$

where p_∞ represents the ambient atmospheric pressure, and r and M denote the distance between the microphone and $\partial\Omega_e$ and the Mach number of the vapor-jet, respectively. It is worth noting that under perturbations, Eq. 2 can be combined with Eq. 1 and obtain

$$p_{acc} - p_\infty = -\frac{\rho_v \phi_e}{4\pi r} (2M + 1) \frac{d^2 L}{dt^2}. \text{ We call Eq. 2 the } \textit{Vapor-jet-Cavity (keyhole) Aeroacoustic Equation}$$

(VCAE), more derivation details of which are referred to the Supplementary Materials. Essentially, VCAE tells us that the measured acoustic signal near the source, whose amplitude depends nonlinearly on \dot{v}_e and M ($v_{e0}/c_0 \approx v_e/c_0$) and decays proportionally to $1/r$, can be interpreted as emission yielded effectively by a monopole and a dipole directed along the vapor ejection axis. For most vapor-cavity cases where $M \ll 1$ (*i.e.*, low v_e regime and no shock-wave involved), the acoustic emission amplitude is dominated by those of the monopole component and thus becomes proportional to \dot{v}_e , which, under steady oscillations, matches the evolution of $-\ddot{L}$. VCAE also serves as a confirmation and extension of the previously investigated laser welding acoustic

mechanism⁸, as well as an alternative interpretation of the *Ffowcs Williams–Hawkings (FW–H) equation*, used in aeroacoustics to predict the noise generated by moving rigid surfaces³⁶. Finally, we emphasize that our analysis treats acoustic emission dominated by vapor-jet unsteadiness. Unless strong vortex shedding occurs near $\partial\Omega_e$, we for now neglect far-field turbulence- and eddy-driven sound better described by classical “jet-noise” models. This distinction clarifies what our airborne acoustics measures near the vapor-jet exit²⁰.

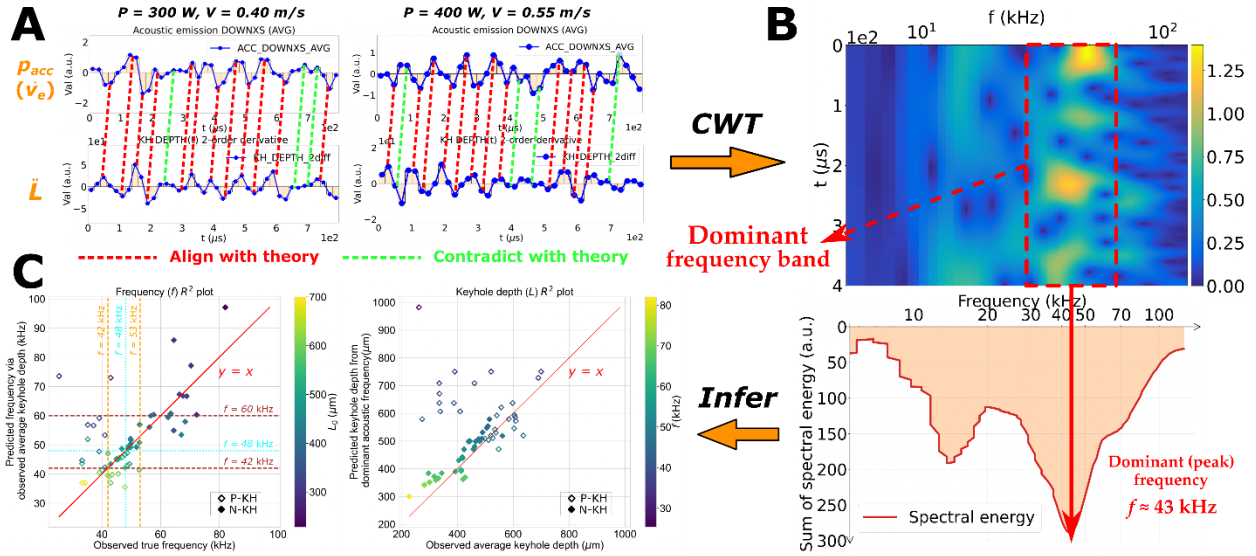


Fig. 2. Discovered correlations between cavity-depth acceleration and measured aeroacoustic signatures enable interpretable inference of vapor-cavity oscillation properties on sub-millisecond timescales. (A) Correlation between the acoustic data (p_{acc} , top row) and the second time-derivative of the measured vapor-cavity depth (\ddot{L} , bottom row) of two example cases. The red dashed lines connecting signals from two independent modalities reveal clear inverse correlation implied by Eq. 1 with a constant phase shift, illustrated by the slope of the dashed lines due to inherent synchronization offset of the data collection system (*i.e.*, around 20–40 μs); while a few point pairs labeled by the green dashed lines contradict the theory due to inevitable noise and arbitrary factors. (B) Data processing that converts time-series data to spectro-temporal scalograms via continuous wavelet transform. From the resultant scalograms, we extracted the highest peak of the energy summation value of each frequency band to represent the dominant acoustic frequency of the corresponding snippet. (C) Predictions of vapor-cavity oscillation characteristics, including oscillation frequency and average cavity depth, across process conditions within 400 μs time window. For each 400 μs snippet, VCODE: (1) uses vapor-cavity geometric features to estimate the oscillation frequency (left), and (2) uses the dominant acoustic frequency to infer the mean cavity depth (right). Solid markers denote N-KHs, and hollow markers denote P-KHs. In the left plot, we observe two critical threshold frequencies (f_c) along each axis (orange and brown dashed lines) that roughly partition the map into three regimes—predominantly P-KHs, predominantly N-KHs, and a mixed region—with a few outliers. Another frequency ($f_c = 48$ kHz, cyan dashed lines) emerges as a critical intersection between N-KHs and P-KHs along the diagonal ($y = x$, red solid line), suggesting the existence of critical frequencies controlling keyhole stability and pore-shedding behaviors.

Guided by Eqs. 1 and 2, we investigate within 800 μs snippets the correlation between the time histories of \dot{v}_e and \ddot{L} , independently extracted and numerically calculated from experiment data of airborne acoustic emissions and side-view X-ray images of vapor cavities. Figure 2A showcases two example snippets with close temporal agreement between the two modalities, revealing that the acoustic signal captures the rate of vapor-jet through $\partial\Omega_e$ and, consequently, the evolution history and dominant frequencies of cavity depth oscillations. Results clearly show that the acoustic amplitude parallels its corresponding cavity depth evolution with the same oscillation frequency and a phase lag. Reconciling with our mechanistic interpretation, the discovered correlation and its associated interpretation enable noninvasive characterization of vapor-jet dynamics and cavity oscillations on sub-millisecond scales, demonstrating the potentials of quantifying vaporization-related properties and parameters by simply using airborne acoustic emission data.

Analysis of the vapor-jet-driven cavity dynamics

We further extend the above analysis to more general pore-free cavity oscillations. Starting from the integral mass and momentum balances over the domain enclosing the vapor cavity and introducing a few simplifying assumptions (see Supplementary Information), we arrive at the following new nonlinear ordinary differential equation for L , which we call the *Vapor-jet-Cavity (keyhole) Oscillation Dynamics Equation (VCODE)*:

$$\rho_v \phi_e (L\ddot{L} + \dot{L}^2) + (2\varphi\rho_v\Omega - \dot{m})\dot{L} + (2\pi C\gamma \cos\theta - \dot{m})L = (p_e + \rho_v v_e^2)\phi_e \quad (\text{Eq. 3})$$

where:

- p_e —local pressure at $\partial\Omega_e$.

- γ, θ —coefficient of surface tension at $\partial\Omega_v$ and the cavity characteristic angle (*e.g.*, can be interpreted as the front wall inclination angle).
- C, φ —phenomenological parameters for interfacial forces at $\partial\Omega_v$ and the vertical vapor-velocity gradient, respectively.

Full derivation details are provided in the Supplementary Information (see Extended Data Fig. S1). Fundamentally, VCODE models the vapor-jet cavity as a vertical closed-end vapor depression column whose depth is under nonlinear oscillations sustained by continuous laser energy input. It is worth noting that $\dot{v}_e = -\ddot{L}$, previously used for perturbative analysis, does not hold at this point, since we don't have $\dot{m} = 0$ anymore. From Eq. 3, we point out the following observations:

1. VCODE captures the interplay between vaporization-induced recoil effects ($(p_e + \rho_v v_e^2)\phi_e$) and depth-dependent restoring actions at $\partial\Omega_v$ ($2\pi C\gamma \cos\theta \cdot L$; more details in the Supplementary Information), the driving forces governing the vapor-cavity oscillation.
2. Additional theoretical analysis (Supplementary Information) further shows that the cavity depth co-oscillates with the acoustic pressure (*i.e.*, same frequency as the driving force), with a damping-dependent phase lag.
3. It introduces a new dynamical-systems perspective: \dot{m} , Ω , \dot{L} , and φ in Eq. 3 regulate whether cavity oscillations decay or grow, providing a mechanistic description that spans energy-dissipating responses and self-amplifying, exponentially growing depth dynamics. As their balance shifts, the damping can vary, cross zero, and change sign, thereby moving the vapor-jet cavity oscillator between stable and unstable regimes and motivating

mechanistic descriptions and further exploration of self-oscillation, nonlinear saturation, and limit-cycle behavior.

4. Mathematically, it not only parallels but also further extends the well-known *Rayleigh–Plesset equation*^{34,35}, which assumes spherical cavity symmetry and is widely used to model bubble oscillations and cavitation in liquids. By instead treating an axisymmetric cavity and explicitly accounting for vapor-velocity gradient and vapor-jet flux along cavity depth, VCODE underscores its novelty and distinction from established physical descriptions of cavity dynamics.

In essence, VCODE describes cavity-depth fluctuations as the motion of a sustained nonlinear oscillator whose properties and transient evolution are governed by geometric factors, material parameters, and boundary variables (*i.e.*, L (\dot{L}), \dot{m} , v_e , θ , γ).

Next, under small perturbations, we substitute $\delta \dot{v}_e = -\delta \ddot{L}$ into Eq. 3 and obtain the following perturbative form of VCODE:

$$\rho_v \phi_e \left[L_0 \delta \ddot{L} + (2\varphi L_0 + v_{e0}) \delta \dot{L} \right] + 2\pi C \gamma \cos \theta_0 \cdot \delta L = 0 \quad (\text{Eq. 4})$$

More details are provided in the Supplementary Information. At a specific moment of perturbative oscillation, Eq. 4 takes the canonical form of a damped oscillator for δL , where the first term corresponds to effective mass inertia ($M = \rho_v \phi_e L_0$), the second term to effective damping ($c = \rho_v \phi_e (2\varphi L_0 + v_{e0})$, where the sign of φ depends on the direction of vapor-velocity gradient),

and the third term to the effective restoring stiffness arising from interfacial actions including capillary surface tensions ($k = 2\pi C\gamma \cos \theta_0$) (shown in Fig. 1C). Under perturbative pore-free oscillation of the cavity depth, an immediate first-order estimate of its frequency is the natural frequency (f_N) derived from Eq. 4, writing as:

$$f_N = \frac{\omega_L}{2\pi} \approx \frac{1}{2\pi} \sqrt{\frac{2\pi C\gamma \cos \theta_0}{\rho_V \Omega_0}} = \sqrt{\frac{C\gamma \cos \theta_0}{2\pi \rho_V \phi_e L_0}} \quad (\text{Eq. 5})$$

Under perturbative cavity oscillations, Eq. 5 serves as an effective linear approximation for the actual cavity depth oscillation frequency, which is related to the material properties and cavity's geometric factors. When damping becomes non-negligible, the actual frequency should be closer to the system's resonant frequency that is considerably smaller than f_N , making it an effective upper bound of the actual vapor-cavity oscillation frequency.

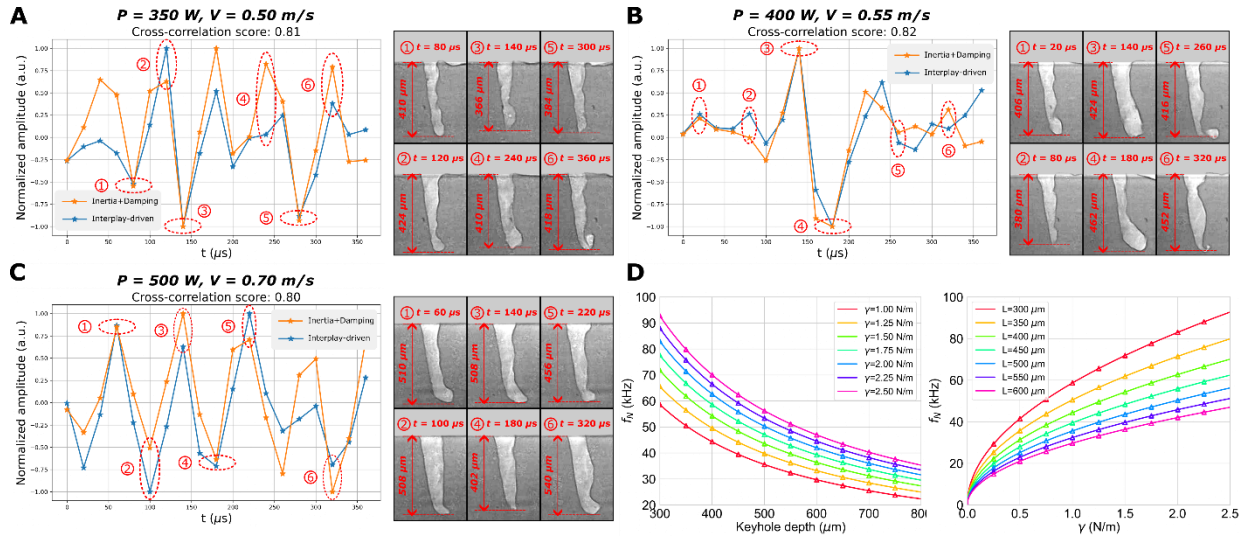


Fig. 3. VCODE-enabled cross-modal agreement over sub-millisecond windows and sensitivity analysis. (A)(B)(C) All measurements in the showcased three snippet subplots are temporally aligned and segmented into 400 μs windows. For each snippet, we compute the normalized *Inertia+Damping* and *Interplay-driven* terms of the VCODE (Eq. 3) using acquired experimental data after synchronization. In the left panel, despite a few mismatching outliers, the geometry-driven and acoustic-driven time traces show consistent trend alignment across different operating conditions. The corresponding X-ray frames annotated with time stamps (the right panel) visualize the cavity

shapes at the labeled points. Similar results have been obtained over a total of fifty snippets across different conditions. **(D)** Sensitivity of estimated natural frequency with respect to average cavity depth (left) and surface tension coefficient (right) according to the proposed theory.

Combining Eqs. 1, 4, and 5, our theory further implies that we can use acoustic frequencies to estimate the actual frequency of the steady perturbative cavity depth oscillation and, in turn, infer the geometric parameters of the cavity itself within sub-millisecond time windows. We demonstrate this potential predictive power of Eq. 5 on experimental data across different process parameters. For each 400 μ s snippet, we either predict the oscillation frequency by substituting cavity geometric features or predict the mean depth by substituting the dominant airborne acoustic frequency obtained from CWT scalograms, shown in Fig. 2B. In Fig. 2C, we demonstrate the inference results of frequency given depth (left) and depth given frequency (right) and summarize the following three major takeaways:

1. For N-KHs (solid markers), theoretical predictions agree with both the dominant acoustic frequencies and X-ray measured mean cavity depths (frequency prediction $R^2 \geq 0.87$, depths prediction $R^2 \geq 0.85$).
2. For P-KHs (hollow markers), predictions degrade as expected, consistent with the imposed limits of validity (see Supplementary Information) that our theory collapses when non-negligible pores are generated.
3. Vapor cavities tend to break down and shed pores within low-frequency resonance regimes.

In the left plot, specifically, we observe two critical threshold frequencies (f_c) along each axis (orange dashed lines—42 kHz and 53 kHz for the observed frequency; and brown dashed lines—42 kHz and 60 kHz for the prediction frequency) that roughly partition the frequency spectrum into three parts based on the cavity types—predominantly P-KHs, predominantly N-KHs, and a mixed region—with a few outliers. Another frequency

($f_c = 48$ kHz, cyan dashed lines) emerges as a critical intersection between N-KHs and P-KHs along the diagonal ($y = x$, red solid line). These frequencies fall within the range previously reported for Ti-6Al-4V vapor-cavity oscillations¹⁹, suggesting a critical vapor-cavity stability threshold that may be governed by resonance of the coupled cavity-liquid system.

We further combine Eq. 3 with experimental measurements to qualitatively validate the proposed VCODE theory. Because converting each sensor modality to absolute physical units is extremely challenging, we instead compare the normalized temporal trends of two aggregated terms: (i) the sum of the nonlinear inertial and damping contributions (*Inertia+Damping*, the first two terms on the left of Eq. 3), and (ii) the net “competitive interplay” defined as the difference between the right-hand side of Eq. 3 and the restoring term (*Interplay-driven*, the right-hand side of Eq. 3 subtracts the last term on the left). This decomposition is motivated by the observation that the *Inertia+Damping* contribution is typically an order of magnitude smaller than the *Interplay-driven* term, so it can be interpreted as a dynamical residual arising from the near-balance between recoil forcing and capillary restoration. We computed the two summation terms purely from experimentally collected data across a series of out-of-sample snippets with different process conditions, evaluating their cross-correlation scores to demonstrate the effectiveness of VCODE. It is worth noting that since we don’t have $\ddot{m} = 0$, we use the auxiliary photodiode modality to capture laser absorption that can be used to infer \dot{m} . As shown in Figs. 3A–3C, we discover and demonstrate that after calibrating phenomenological parameters in Eq. 3 using only one $400 \mu\text{s}$ snippet, *Inertia+Damping* and *Interplay-driven* terms show consistent trend alignment across

three snippets encompassing different P – V settings. The results of more snippets are available in the Supplementary Information (Extended Data Fig. S2).

Finally, we perform sensitivity analysis using Eqs. 4 and 5 regarding how f_N changes with varying vaporization parameters. Figure 3D clearly shows that f_N decreases with increasing cavity depth and decreasing γ ; from Eq. 5, we also realize that f_N should increase with decreasing θ . Theoretically, $\cos \theta$ depends on the aspect ratio of the keyhole ($L/2R$, $\phi_e = \pi R^2$) (see Supplementary Information); from a physical perspective, however, we can interpret θ as the vapor-cavity front-wall inclination angle, which sets the direction of capillary forces along the front wall and does not materially affect the interpretation of VCODE. Therefore, these observations link the frequency of cavity-depth fluctuations to geometric parameters and liquid-vapor interfacial properties, providing new perspectives for a physics-based understanding of cavity oscillations that can, in turn, govern defect formation¹⁹. The implications and impacts of this observation will be further discussed in the next section.

Implications and impacts in metallic additive manufacturing

Additional analyses—including a dimensionless stability number for the vapor-jet-driven open cavity and the correspondence between acoustic and thermal signatures—are provided in the Supplementary Information (Extended Data Figs. S3–S6). Collectively, they support a mechanistic picture of the vapor-jet-cavity as a damped, driven dynamical system: cavity depth behaves as a lossy resonator continuously forced by vapor-jet/recoil-pressure fluctuations. In this regime, the cavity response is frequency-locked to dominant forcing components, while broadband excitation

is preferentially amplified near the cavity's resonant band. Because the airborne acoustic field is generated by (and radiated approximately linearly from) the same unsteady jet and pressure field that both drives and responds to cavity motion, the emitted tone inherits the system's dominant response frequency. Accordingly, under conditions where cavity depth is governed by nonlinear coupled oscillations, the dominant acoustic tone near the cavity exit tracks the transient cavity-depth oscillation frequency, with a damping-induced phase lag between forcing and response. This coupling generalizes across materials, as shown by AlSi10Mg bare-plate measurements (Extended Data Fig. S3; Extended Data Video S1) and by cross-correlation analyses between cavity-depth and acoustic-amplitude evolutions (mean absolute correlation > 0.6 ; Extended Data Fig. S4; Extended Data Videos S1–S3). Together, these results clarify the physical origins of the measured signals and establish sub-millisecond, deterministic links among vapor-jet dynamics, cavity oscillations, and airborne acoustics—enabling accurate, rapid (few-hundred-microsecond) and low-cost, noninvasive inference of cavity depth and oscillation frequency from airborne measurements.

To extend the impact of this work and further illustrate the broader implications of our theory, we contextualize the newly developed framework in laser-PBF, a widely adopted LMP and additive manufacturing technique in which intense vaporization is common, to explore further implications and practical applications. We utilize the newly identified thresholding keyhole oscillation frequency in Fig. 2C and VCODE formulations to construct a new interpretation of the established KH-bound state. As shown in Fig. 4A, inspired by Eq. 5 and based on the data measured and extracted from X-ray synchrotron images, we discovered that experimentally derived quantities,

namely $\frac{\cos \theta}{L}$ vs. $\frac{P - P_0}{V^n}$ (in Fig. 4A, we have $n=4$ and $P_0 = 50$ W for Ti-6Al-4V from experiments, where P_0 denotes the maximum zero-scan-speed power for pore-free keyhole oscillation and is introduced based on the fact that there always exists such a non-zero keyhole depth when V vanishes), exhibit a strong reciprocal relationship. Motivated by the observation in Fig. 2C, we hypothesize a single critical keyhole oscillation frequency, f_c , whose iso-frequency contour in the P - V space delineates the keyhole-defect regime and defines the corresponding process window. Assuming that all N-KHs remain in the perturbative-oscillation regime until they become unstable and transition to P-KHs, we use f_N from Eq. 5 to estimate f_c at the critical boundary. By keeping n as an undetermined parameter and substituting $\frac{\cos \theta}{L} = B \frac{V^n}{P - P_0} + b$ (where B and b are fitting constants with specific units) into Eq. 5, we obtain:

$$P = \frac{BC\gamma}{2\pi\rho_V\phi_e f_c^2 - bC\gamma} V^n + P_0 \quad (\text{Eq. 6})$$

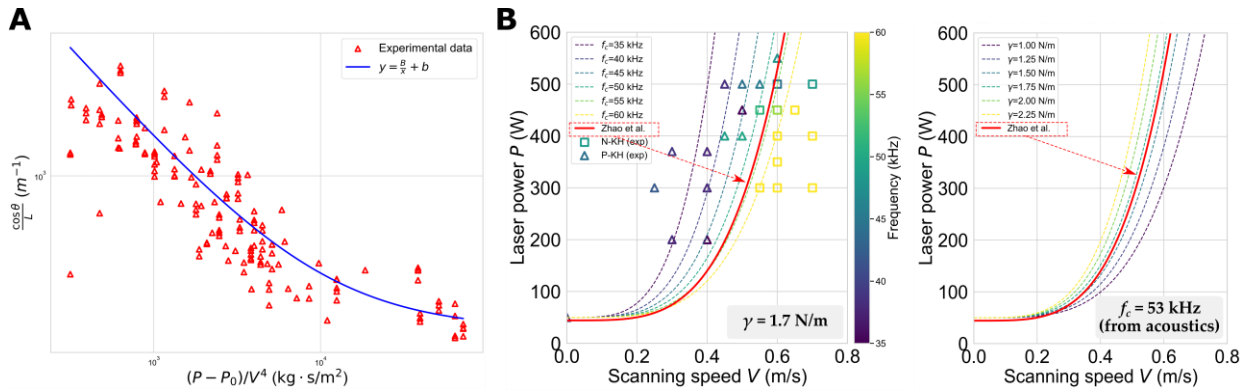


Fig. 4. Experimentally discovered interpretation, scaling, and modeling of the KH-bound and vapor keyhole frequency threshold. (A) Experimental measurements show the inversely proportional empirical relationship (with constants B and b) between two ratios derived from (with $n = 4$) collected data as a log-log plot. The corresponding fitting parameters as well as state variables are listed in the Supplementary Information and will be used for the visualization of Eq. 6. Red triangular markers denote the data points, and the blue curve is a best-fit inverse function. (B) Interpretation of the KH-bound as an iso-frequency contour in the P - V space. We plot the KH-bound reported by Zhao *et al.*¹⁹ (red), meanwhile superimposing iso-frequency contours with $n = 4$ and examining their sensitivities with respect to varying f_c and γ . Specifically, these iso-frequency contours are obtained: (1) for f_c ranging from 35–60

kHz (left, with γ fixed near that of liquid Ti-6Al-4V at its boiling point, *i.e.*, $\gamma \approx 1.7$ N/m), and the result shows that the reported boundary aligns closely with the $f_c = 53$ kHz contour, matching what we observed from the experiments; (2) for γ ranging from 1–2.25 N/m (right, with $f_c = 53$ kHz). Moreover, we scatter in the left plot datapoints of acoustic frequency (annotated with colors) measured for both P-KHs (triangular markers) and N-KHs (square markers) from multimodal experiments of different P – V conditions; we observe a general frequency gradient perpendicular to the visualized iso-frequency contours. These findings provide potential explanations and interpretations for the experimentally characterized KH-bound in LMP and specifically laser-PBF community.

We observe that Eq. 6 reveals a polynomial relationship between P and V on the KH-bound, a general mathematical expression of the iso-frequency contour in the P – V space that corresponds to the hypothesized f_c . As shown in Fig. 4B, when using fitted parameters from Fig. 4A and Figs. 3A–3C, $n = 4$, and specific material parameters of Ti-6Al-4V ($\gamma = 1.7$ N/m), the superimposed KH-bound reported by Zhao *et al.*¹⁹ closely agrees with the iso-frequency contour corresponding to $f_c = 53$ kHz, matching one of the thresholding frequencies independently found in Fig. 2C. In the left plot of Fig. 4B, we scatter datapoints of acoustic frequency (annotated with colors) measured for both P-KHs (triangular markers) and N-KHs (square markers) from multimodal experiments of different P – V conditions, demonstrating a general frequency gradient perpendicular to the visualized iso-frequency contours. Furthermore, Fig. 4B also showcases how the KH-bound may vary in the P – V space when we change γ or f_c . Aside from the above, this result also links to a recent study³⁷, which reported that the KH-bound depends on keyhole aspect ratio and inclination angle, consistent with our prediction of a critical iso-frequency contour related to the same quantities. Accordingly, Eq. 6 offers a theoretical basis for the KH-bound and yields an interpretable process map that can guide parameter selection and optimization.

From a mechanistic perspective, VCODE offers an alternative physical picture of keyhole oscillations. As shown in Eqs. 3 and 4, VCODE essentially describes the vapor-jet–cavity as a

nonlinear oscillatory dynamical system; the effective damping coefficient of this system, namely $(2\phi\rho_v\Omega - \dot{m})$ or $\rho_v\phi_e(2\phi L_0 + v_{e0})$, is fundamentally controlled by (1) the direction of vapor-velocity gradient and (2) the relation between \dot{m} and L (see Supplementary Information). In other words, this effective damping coefficient can take either positive (energy-dissipating) or negative signs (energy-injecting) depending on the transient status of the vapor-jet–cavity system, thereby capturing different keyhole dynamics regimes. When the damping coefficient crosses zero, system trajectories may transition from self-amplifying exponential growth to nonlinear saturation, potentially restabilizing into bounded oscillations or abruptly collapsing, producing pores and resetting the keyhole state.

Notably, during collapse, uncontrolled pore evacuation can violate the strict mass-conservation assumptions, stating the theory’s domain of validity: quasi-axisymmetric keyholes with negligible mass loss to pores satisfy the assumptions; whereas extremely shallow cavities, strongly asymmetric geometries, or conditions with significant pore ejection violate mass conservation and lie outside its scope. What’s more, we showed that \dot{m} can be inferred indirectly from photodiode-based laser-reflection measurements, because it depends strongly on the total laser absorption within the cavity, which in turn is governed by the evolving cavity geometry and absorptivity. We identify the above as key limitations and avenues for future work, where additional modeling concepts and sensing modalities, such as self-excited oscillations, chaotic dynamics, or sophisticated photodiode sensing, may be required to capture unstable vapor cavity behaviors.

More broadly, we believe this work lays a general physical foundation for cost-efficient physical characterization of vapor-jet–cavity dynamics during intense evaporation, which arises across a wide range of scientific and engineering settings^{2–8}. With the support of the new theoretical framework and synchronized observations from our vaporization prototype, airborne emissions can be elevated from qualitative indicators to quantitative, physics-informed observables that recover key dynamical variables and stability-relevant thresholds. Moreover, the coupled modeling strategy developed here—linking first-principles cavity dynamics with aeroacoustic radiation and validating the mapping against time-resolved geometry—offers a transferable route for interrogating other non-equilibrium vaporization systems in which driven vapor jets interact with compliant liquid-vapor interfaces. This perspective opens opportunities for scalable monitoring, interpretable process conditionings, and feedback-ready control strategies in vaporization-mediated manufacturing and beyond.

Conclusions

We recast ubiquitous aeroacoustic signatures from intense laser-induced vaporizations into cost-effective microsecond-level probes of transient vapor-cavity depth acceleration and cavity oscillation frequency, enabling a noninvasive and scalable route to resolve extremely fast vapor-jet-driven cavity dynamics. Building on this observability, we develop the *Vapor-jet–Cavity (keyhole) Oscillation Dynamics Equation* (VCODE), which models the excessive-vaporization cavity as a nonlinear dynamical system whose depth fluctuations regulate vapor ejection and radiated sound. VCODE linearization yields predictive expressions for oscillation frequency, amplitude, and stability. Coupling VCODE with aeroacoustic formulations leads to the *Vapor-jet–Cavity (keyhole) Aeroacoustic Equation* (VCAE), which connects vapor-ejection kinematics to

measurable acoustic pressure near the cavity exit. Synchronized operando experiments validate predictions from VCODE and VCAE, showing that airborne acoustics enable accurate inference of keyhole oscillation frequency and mean depth in pore-free regimes within sub-millisecond windows (frequency: $R^2 \geq 0.87$; depth: $R^2 \geq 0.85$). We further identify stability-relevant thresholding frequencies that delineate pore-shedding from pore-free keyhole behavior. Together, these results establish a physics-based foundation for real-time, control-relevant inference of vapor-jet-driven cavity dynamics in metal additive manufacturing.

Our framework supports a deterministic dynamical-systems view in which vapor cavities behave as nonlinear, self-sustained oscillators, and their acoustic emissions encode internal state variables that can be recovered from airborne measurements within a well-defined validity regime. Within this regime, the KH-bound results establish quantitative stability delineations—via critical thresholding frequencies that separate pore-free perturbative oscillations from pore-shedding or collapse-prone behaviors—thereby providing an interpretable map of operating conditions and actionable margins for process design. Finally, the coupled strategy advanced, *i.e.*, deriving first-principles cavity dynamics, linking them to aeroacoustic radiation, and validating that mapping against time-resolved geometry, offers a transferable route for quantitative, cost-efficient characterization of other non-equilibrium vaporization systems in which driven vapor jets interact with compliant liquid–vapor interfaces, enabling interpretable monitoring and feedback-ready control beyond laser powder bed fusion.

References

1. M. Minnaert, XVI. On Musical Air-Bubbles and the Sounds of Running Water. *The London, Edinburgh, and Dublin Philosophical Magazine and Journal of Science* **16** (104), 235–248 (1933).
2. T. G. Leighton, *The Acoustic Bubble* (Academic Press, 1994).
3. C. E. Brennen, *Cavitation and Bubble Dynamics* (Oxford University Press, 1995).
4. P. Wu, X. Wang, W. Lin, L. Bai, Acoustic characterization of cavitation intensity: A review. *Ultrason. Sonochem.* **82**, 105878 (2022).
5. A. Vogel, V. Venugopalan, Mechanisms of Pulsed Laser Ablation of Biological Tissues. *Chemical Reviews* **103**, 577–644 (2003).
6. L. Grad, J. Grum, I. Polajnar, J. M. Slabe, Feasibility study of acoustic signals for on-line monitoring in short circuit gas metal arc welding. *International Journal of Machine Tools and Manufacture* **44**, 555–561 (2004).
7. J. Horvat, J. Prezelj, I. Polajnar, M. Čudina, Monitoring Gas Metal Arc Welding Process by Using Audible Sound Signal. *Strojniški vestnik - Journal of Mechanical Engineering* **57**, 267–278 (2011).
8. D. F. Farson, K. R. Kim, Generation of Optical and Acoustic Emissions in Laser Weld Plumes. *Journal of Applied Physics* **85**, 1329–1336 (1999).
9. A. U. Rehman, M. A. Mahmood, F. Pitir, M. U. Salamci, A. C. Popescu, I. N. Mihailescu, Keyhole formation by laser drilling in laser powder bed fusion of Ti6Al4V biomedical alloy: Mesoscopic computational fluid dynamics simulation versus mathematical modelling using empirical validation. *Nanomaterials* **11**, 3284 (2021).

10. Y. Huang, T. G. Fleming, S. J. Clark, S. Marussi, K. Fezzaa, J. Thiyagalingam, C. L. A. Leung, P. D. Lee, Keyhole fluctuation and pore formation mechanisms during laser powder bed fusion additive manufacturing. *Nat. Commun.* **13**, 1170 (2022).
11. L. Guo, H. Wang, H. Liu, Y. Huang, Q. Wei, C. L. A. Leung, Y. Wu, H. Wang, Understanding keyhole induced-porosities in laser powder bed fusion of aluminum and elimination strategy. *Int. J. Mach. Tools Manuf.* **184**, 103977 (2023).
12. M. Grasso, B. M. Colosimo, Process defects and in situ monitoring methods in metal powder bed fusion: A review. *Meas. Sci. Technol.* **28**, 044005 (2017).
13. R. McCann, M. A. Obeidi, C. Hughes, É. McCarthy, D. S. Egan, R. K. Vijayaraghavan, A. M. Joshi, V. A. Garzon, D. P. Dowling, P. J. McNally, D. Brabazon, In-situ sensing, process monitoring and machine control in Laser Powder Bed Fusion: a review. *Addit. Manuf.* **45**, 102058 (2021).
14. H. Liu, C. Gobert, K. Ferguson, B. Abranovic, H. Chen, J. L. Beuth, A. D. Rollett, L. B. Kara, Inference of highly time-resolved melt pool visual characteristics and spatially-dependent lack-of-fusion defects in laser powder bed fusion using acoustic and thermal emission data. *Addit. Manuf.* **83**, 104057 (2024).
15. C. Zhao, K. Fezzaa, R. W. Cunningham, H. Wen, F. De Carlo, L. Chen, A. D. Rollett, T. Sun, Real-time monitoring of laser powder bed fusion process using high-speed X-ray imaging and diffraction. *Sci. Rep.* **7**, 3602 (2017).
16. S. A. Khairallah, T. Sun, B. J. Simonds, Onset of periodic oscillations as a precursor of a transition to pore-generating turbulence in laser melting. *Additive Manufacturing Letters* **1**, 100002 (2021).

17. A. A. Martin, N. P. Calta, S. A. Khairallah, J. Wang, P. J. Depond, A. Y. Fong, V. Thampy, G. M. Guss, A. M. Kiss, K. H. Stone, C. J. Tassone, J. Nelson Weker, M. F. Toney, T. van Buuren, M. J. Matthews, Dynamics of pore formation during laser powder bed fusion additive manufacturing. *Nat. Commun.* **10**, 1987 (2019).
18. Z. Ren, L. Gao, S. J. Clark, K. Fezzaa, P. Shevchenko, A. Choi, W. Everhart, A. D. Rollett, L. Chen, T. Sun, Machine learning–aided real-time detection of keyhole pore generation in laser powder bed fusion. *Science* **379**, 89–94 (2023).
19. C. Zhao, N. D. Parab, X. Li, K. Fezzaa, W. Tan, A. D. Rollett, T. Sun, Critical instability at moving keyhole tip generates porosity in laser melting. *Science* **370**, 1080–1086 (2020).
20. I. Bitharas, N. Parab, C. Zhao, T. Sun, A. D. Rollett, A. J. Moore, The interplay between vapour, liquid, and solid phases in laser powder bed fusion. *Nat. Commun.* **13**, 2959 (2022).
21. J. R. Tempelman, A. J. Wachtor, E. B. Flynn, P. J. Depond, J. B. Forien, G. M. Guss, N. P. Calta, M. J. Matthews, Detection of keyhole pore formations in laser powder-bed fusion using acoustic process monitoring measurements. *Addit. Manuf.* **55**, 102735 (2022).
22. X. Peng, A. I. Nazari, A. P. Steuerma, Y. Zhang, A. K. Prashanth, S. S. Sampath, A Review of In Situ Defect Detection and Monitoring Methods in Selective Laser Melting. *Mater. Des.* **238**, 112620 (2024).
23. Z. Ren, J. Shao, H. Liu, S. J. Clark, L. Gao, L. Balderson, K. Mumm, K. Fezzaa, A. D. Rollett, L. B. Kara, T. Sun, Sub-millisecond keyhole pore detection in laser powder bed fusion using sound and light sensors and machine learning. *Mater. Futures* **3**, 045001 (2024).
24. M. Hamidi Nasab, G. Masinelli, C. de Formanoir, L. Schlenger, S. Van Petegem, R. Esmailzadeh, R. E. Logé, Harmonizing sound and light: X-ray imaging unveils acoustic

- signatures of stochastic inter-regime instabilities during laser melting. *Nat. Commun.* **14**, 8008 (2023).
25. F. Tenner, D. Riegel, E. Mayer, M. Schmidt, Analytical model of the laser welding of zinc-coated steel sheets by the aid of videography. *J. Laser Appl.* **29**, 022411 (2017).
26. M. Luo, R. Hu, Q. Li, A. Huang, S. Pang, Physical understanding of keyhole and weld pool dynamics in laser welding under different water pressures. *Int. J. Heat Mass Transf.* **137**, 328–336 (2019).
27. P. Ferro, L. Romanin, F. Berto, Understanding powder bed fusion additive manufacturing phenomena via numerical simulation. *Frattura ed Integrità Strutturale* **14**, 252–284 (2020).
28. Y. Sun, S. Gorgannejad, A. A. Martin, N. P. Calta, M. Kiss, J. Wang, M. Jacquemet, M. J. Matthews, Direct mechanistic connection between acoustic signals and melt-pool morphology during laser powder bed fusion. *Applied Physics Letters* **125**, 034102 (2024).
29. J. Lighthill, Early development of an “acoustic analogy” approach to aeroacoustic theory. *AIAA J.* **20**, 449–450 (1982).
30. M. J. Lighthill, On sound generated aerodynamically. I. General theory. *Proc. R. Soc. Lond. A* **211**, 564–587 (1952).
31. O. Ronneberger, P. Fischer, T. Brox, “U-Net: Convolutional Networks for Biomedical Image Segmentation” in *Medical Image Computing and Computer-Assisted Intervention – MICCAI 2015*, N. Navab, J. Hornegger, W. M. Wells, A. F. Frangi, Eds. (Springer, Cham, 2015), vol. **9351** of *Lecture Notes in Computer Science*, pp. 234–241.
32. Materials and methods are available as supplementary materials.

33. Y. Zhang, S. Wu, Z. Guo, G. Peng, L. Wang, W. Yan, Defects caused by powder spattering and entrainment in laser powder bed fusion process: High-fidelity modeling of gas, melt pool and powder dynamics. *Acta Mater.* **288**, 120816 (2025).
34. L. Rayleigh, On the pressure developed in a liquid during the collapse of a spherical cavity. *Philosophical Magazine* **34**, 94–98 (1917).
35. M. S. Plesset, The dynamics of cavitation bubbles. *Journal of Applied Mechanics* **16**, 277–282 (1949).
36. S. Mendez, M. Shoeybi, S. K. Lele, P. Moin, On the use of the Ffowcs Williams–Hawkings equation to predict far-field jet noise from large-eddy simulations. *Int. J. Aeroacoust.* **12**, 1–20 (2013).
37. E. Ruckh, R. Lambert-Garcia, S. Hocine, A. C. M. Getley, C. Iantaffi, A. Bhatt, M. Fitzpatrick, S. Marussi, A. Farndell, T. Schubert, G. Ketzer-Raichle, M. Majkut, A. Rack, N. Jones, C. L. A. Leung, P. D. Lee, Process mapping of Ti-6Al-4V laser powder bed fusion using in situ high-speed synchrotron X-ray imaging. *Addit. Manuf.* **113**, 105007 (2025).

Methods

Vapor-jet-cavity prototype based on laser-induced evaporation

Controllable laser-induced evaporation were performed on metallic alloy using a modulated, steerable fiber laser (maximum power 700 W, wavelength 1064 nm) with a Gaussian beam profile and an 82 μm focal-spot diameter. Experiments were conducted using a focused laser across a range of power–scan speed (P – V) combinations to systematically probe vapor-cavity behavior. The scan length was 4 mm when the laser traveling speed was non-zero. The experimental

environment was a closed airtight chamber, filled with argon at atmospheric pressure and oxygen level <100 ppm. The substrate material, dimensions, and surface preparation were: Ti-6Al-4V alloy and AlSi10Mg alloy, 50 mm × 5 mm × 0.5 mm, with all surfaces well-polished up to P800.

Synchronized multimodal *in situ* diagnostics

A synchronized sensing suite captured complementary process responses across timescales and spatial resolutions, including: (i) an ultrasonic microphone sampled at 1 MHz to record airborne ultrasonic emissions; (ii) a photodiode sampled at 1 MHz to monitor laser reflection; (iii) a near-infrared (NIR) thermal camera operated at 250 kfps with 1 μs exposure to resolve melt-pool and cavity-opening dynamics; and (iv) high-speed synchrotron X-ray radiography operated at 50 kfps with 2 μs exposure and 2 μm/pixel to directly visualize cavity geometry evolution.

The ultrasonic microphone (PCB Piezotronics, model 378C01) was positioned near the top of the fusion zone to capture near-source acoustic signals from vapor jets exiting the cavity while minimizing turbulence contamination. The microphone was placed approximately 5 mm from the fusion spot. The microphone was mounted at the top of the plate, oriented nearly perpendicular relative to the vapor exit surface. Raw acoustic time series were digitized at 1 MHz using the NIST-DAQ system.

A photodiode was used to monitor laser reflection at a roughly 50° reception angle. The spectral filtering was a 1064 nm bandpass filter for the collection of laser reflections. The photodiode signal was digitized at 1 MHz on the same acquisition system as the acoustic channel. The photodiode voltage was used as a relative measure of reflected intensity.

Synchrotron X-ray radiography. Side-view high-speed X-ray radiography was conducted at the Advanced Photon Source (beamline 32-ID) to visualize transient cavity geometry at 50 kfps ($2 \mu s$ exposure, $2 \mu m$ /pixel). The imaging plane was aligned to capture the cavity; the angle between scan direction and the imaging plane was 90° . NIR thermal imaging was performed using a high-speed camera operated at 250 kfps with $1 \mu s$ exposure. The NIR signal was interpreted as relative thermal intensity.

Timing, triggering, and synchronization. All sensor channels were registered onto a common global timeline to enable direct correlation between acoustic emissions and X-ray-resolved cavity geometry. Triggering hardware was achieved via a manual switch. To account for acoustic time-of-flight from the effective vibration source near the cavity's opening to the microphone, an approximately $15 \mu s$ temporal correction was applied to the acoustic channel. After synchronization, the registered measurements were segmented into short snippets of duration $400 \mu s$ (and, when noted, $800 \mu s$) for subsequent correlation analysis. Snippet start times were selected along the scanning path. Snippets used for calibration were defined as the initial snippets in each dataset, and independent validation used separate snippets not included in calibration.

Multimodal data processing analysis

Acoustic time–frequency analysis. Airborne acoustic signals were analyzed in the time domain and, when needed, using continuous wavelet transforms (CWT) to obtain time–frequency scalograms and extract dominant frequencies and spectro-temporal features. The preprocessing applied prior to CWT (detrending, filtering, normalization) was deseasonalization, which removes

obvious global trends/DC components. The wavelet family selected was Morlet, and the analyzed frequency range and frequency sampling were 5–100 kHz. All signal processing was implemented using ImageJ, Python, and MATLAB Wavelet Toolbox.

X-ray segmentation and geometric feature extraction. Cavity geometries were segmented from synchrotron X-ray images using a U-Net-based convolutional neural network trained on manually annotated frames. The inference pipeline produced binary masks of the vapor cavity for each frame. From segmented masks, we quantified instantaneous characteristic length (depth) of the cavity, opening area, and inclination. Cavity depth was defined as the distance between the vapor cavity exit and the bottom pixel belonging to the detected cavity geometry. Opening area was defined as the area of a circle with a diameter equal to the opening width, and inclination was defined as the slope of the front wall. Mask postprocessing (morphological operations, contour smoothing, removal of spurious regions) was implemented using Python. Measurement uncertainty was assessed by the intersection-over-union and the Dice score, and the resulting geometric time series were co-registered with the acoustic and photodiode signals.

Cross-modality correlation and model validation. Co-registered time series were used for correlation analysis and model validation. Numerical derivatives of the depth signal (*e.g.*, velocity and acceleration) were computed using the Python SciPy package. Cross-correlation analysis between acoustic pressure and depth-derived metrics used cross-correlations, with lag search bounds of 10 μ s. Calibration was performed on one reference snippet, and predictive performance was reported on independent validation snippets. According to VCAE, we have for low-Mach jet flow $p_{acc} \propto \dot{v}_e$. In both perturbative and finite nonlinear vapor-jet-driven cavity oscillations, the

fluctuation magnitude of v_e is no bigger than its long-time-average, *i.e.*, v_{e0} . Therefore, we substitute phase-shifted airborne acoustic signals to v_e -dependent terms—such as v_e or v_e^2 —in JCODE for corresponding qualitative analysis since \dot{v}_e mathematically shares the same frequency and variational trend with $v_e = v_{e0} + A_{v_e} e^{i\omega_e t}$ ($v_{e0} \geq A_{v_e}$) as well as v_e^2 . The inverse of photodiode-collected laser-reflection signal is substituted qualitatively as \dot{m} . Fluctuations in vapor-jet-driven cavity features can be measured either by X-ray imaging of the cavity–compliance profile or by thermal/NIR imaging of the emerging jet at the cavity exit; the resulting oscillation frequency tracks the cavity’s compliance (“breathing”) evolutions and agrees with the acoustic dominant frequency, consistent with our new VCODE/VCAE framework and useful for the subsequent physics-guided quantitative inference with sub-millisecond time window.

Data and materials availability

All data needed to evaluate the conclusions are available in the main text and Supplementary Information (Supplementary Figures 1-6 and Supplementary Table 1). Supplementary Data 1 (data_S1.zip) contains the processed datasets used for figures and model validation. Supplementary Videos 1-3 (movie_S1.mp4-movie_S3.mp4) provide representative synchronized recordings. Raw X-ray radiography and raw acoustic time series are available from the corresponding authors upon reasonable request.

Code availability

Custom code used for acoustic time-frequency analysis, X-ray segmentation, parameter identification, and acoustic-to-state inference is available from the corresponding authors upon reasonable request.

Acknowledgements

We thank **K. Mumm** and **L. Balderson** for assistance with the Advanced Photon Source beamline experiments. We thank **C. Li, R. Jiang, K. Ferguson, X. Li, J. Malen, S. Feng, S. Khairallah, N. Calta, J. Cao, Y. J. Zhang, A. Myer, Y. Sun, I. Matthews, D. Wu, N. Lamprinakos, J. Beuth, T. Reddy, and Z. Taylor** for helpful discussions. We thank **V. Rajan** for assistance with dataset preparation and **S. Liu** for support. This research was performed on APS beam time award(s) (DOI: 10.46936/APS-184522/60012099) from the **Advanced Photon Source**, a U.S. Department of Energy (DOE) Office of Science user facility operated for the DOE Office of Science by **Argonne National Laboratory** under Contract No. **DE-AC02-06CH11357**. **Z. R.** acknowledges partial efforts at the **18-ID (FXI) beamline** of the **National Synchrotron Light Source II (NSLS-II)**, a U.S. DOE Office of Science User Facility operated for the DOE Office of Science by **Brookhaven National Laboratory** under Contract No. **DE-SC0012704**.

Fundings

Eaton Corporation Award Number **001145471** (HL, ADR, LBK).

MIT Postdoctoral Fellowship Program for Engineering Excellence (**PFPFEE**) (SKN).

A*STAR MTC Individual Research Project **M24N7c0082** (WY, YZ).

National Science Foundation grants **DMS 2108784** and **DMREF 1921857** (KD).

Army Research Office MURI **W911NF-24-2-0184** (KD).

Author contributions

Conceptualization: HL, ADR, LBK;

Methodology: HL, SKN, ZR, YZ, JS, SJC, KF, XZ, LG, WY, NW, KD, TS, ADR, LBK;

Investigation: HL, SKN, ZR, YZ, JS, SJC, KF, XZ, LG, NW, KD, TS, ADR, LBK;

Resources and experiments: HL, ZR, SJC, KF, LG, TS, ADR;

Visualization: HL, SKN, ZR, YZ, XZ;

Funding acquisition: KD, WY, TS, ADR, LBK;

Project administration: HL, TS, ADR, LBK;

Supervision: HL, NW, KD, WY, TS, ADR, LBK;

Writing – original draft: HL, SKN, ZR, ADR, LBK;

Writing – review & editing: HL, SKN, ZR, YZ, JS, SJC, KF, XZ, LG, WY, NW, KD, TS, ADR, LBK.

Competing interests

The authors declare that they have no competing interests.